



This is the accepted manuscript made available via CHORUS. The article has been published as:

## Quantifying spin Hall topological Hall effect in ultrathin math

$$\frac{T_m}{\mu_0} \frac{3}{\mu_0} \frac{5}{\mu_0} \frac{12}{\mu_0} \frac{O}{Pt}$$
 bilayers

T. Nathan Nunley, Side Guo, Liang-Juan Chang, David Lujan, Jeongheon Choe, Shang-Fan Lee, Fengyuan Yang, and Xiaoqin Li

Phys. Rev. B **106**, 014415 — Published 22 July 2022

DOI: [10.1103/PhysRevB.106.014415](https://doi.org/10.1103/PhysRevB.106.014415)

# Quantifying Spin-Hall Topological Hall Effect in Ultrathin $\text{Tm}_3\text{Fe}_5\text{O}_{12}/\text{Pt}$ Bilayers

T. Nathan Nunley,<sup>1,2</sup> Side Guo,<sup>3</sup> Liang-Juan Chang,<sup>1,4</sup> David Lujan,<sup>1,2</sup>  
Jeongheon Choe,<sup>1,2</sup> Shang-Fan Lee,<sup>4</sup> Fengyuan Yang,<sup>3,\*</sup> and Xiaoqin Li<sup>1,2,\*</sup>

<sup>1</sup>*Department of Physics, Center of Complex Quantum Systems, The University of Texas at Austin, Austin, Texas 78712 USA*

<sup>2</sup>*Center for Dynamics and Control of Materials and Texas Materials Institute,  
The University of Texas at Austin, Austin, Texas 78712, USA*

<sup>3</sup>*Department of Physics, The Ohio State University, Columbus, Ohio 43210, USA*

<sup>4</sup>*Institute of Physics, Academia Sinica, Taipei, 11529, Taiwan*

(Dated: June 1, 2022)

Recent reports have shown that thulium iron garnet (TmIG) based bilayers are promising material platforms for realizing small, room-temperature skyrmions. For potential applications, it is imperative to accurately evaluate electrical read-out signals of skyrmions. In this context, the topological Hall effect has been considered as a characteristic signature of skyrmion formation. Unlike previous studies that have modeled the anomalous Hall effect in ultrathin TmIG/Pt bilayers, we isolate its contribution to the electrical read-out signal by directly measuring the magnetic hysteresis loops using a sensitive Sagnac magneto-optical Kerr effect technique. Our combined optical and electrical measurements reveal that the spin-Hall topological Hall resistivity is considerably larger than previously estimated values. Our finding further indicates that skyrmions can exist at room-temperature and near-zero applied magnetic fields.

## I. INTRODUCTION

Skyrmions are an increasingly important topic both for the fundamental science of magnetism and for the next generation spintronic technology [1–5]. These topologically protected, chiral spin textures were first observed in the B20 class of crystals [2, 6–8] and later found in common polycrystalline magnetic multilayers with large interfacial Dzyaloshinskii-Moriya interactions (DMI) (e.g. CoFeB/Pt) [3, 9–14]. The ideal characteristics of skyrmions (i.e., small size, room temperature stability, and zero external magnetic field), however, have not been realized in a single material [3, 15]. Epitaxially grown magnetic garnets, e.g.  $\text{Tm}_3\text{Fe}_5\text{O}_{12}$  (TmIG), are among the most promising ferrimagnetic insulators for hosting skyrmions with optimal characteristics. These films exhibit low damping, high crystalline quality with low pinning density [16, 17], interfacial DMI [17–19], and strain-tunable anisotropy [20–26]. They have Curie temperatures well above room temperature but not so large as to prohibit the formation of small skyrmions.

In addition to efficient current induced switching [27, 28] and fast domain wall motion [17, 29, 30], a prominent and highly tunable spin-Hall topological Hall (SH-TH) effect (also called transverse spin Hall magnetoresistance) has been reported in TmIG/heavy-metal bilayers, where electrons in the heavy metal layer adjust their local spins adjacent to the skyrmion spin-textures, yielding an unusual transverse resistivity term proportional to the spin winding number in real space. [19–23]. This topological Hall transverse resistivity have been successfully correlated with skyrmions in other materials. For example, electrical measurements [2], neutron scattering [6],

Lorentz transmission electron microscopy [12, 31], and magnetic force microscopy [3, 4, 10, 11], among other techniques, have been used to establish this correlation in B20 compounds and metallic ferromagnetic multilayers. Many imaging techniques cannot be readily applied to visualize nanometer-sized skyrmions in ultrathin insulating films due to limited sensitivity. Thus, developing a reliable electric read-out method becomes even more critical. As an essential step, one should properly separate several contributions to the Hall signal, i.e., the ordinary Hall (OH), anomalous Hall (AH), and topological Hall (TH) effects [32].

Typically, the anomalous Hall contribution is evaluated by measuring the magnetic hysteresis loop using either vibrating sample magnetometry, or SQUID [8, 33]. However, these techniques do not offer sufficient sensitivity to characterize ultrathin TmIG films with relatively weak magnetization in the few nanometer thickness regime. Less reliable alternatives, such as longitudinal transport or simple modelling, have been used to estimate the spin-Hall anomalous Hall (SH-AH) effect in TmIG/Pt bilayers [20, 23]. An accurate characterization of the SH-AH signal in ultrathin magnetic insulator based bilayers remains critically missing.

In this paper, we address this critical need by applying a highly sensitive magneto-optical Kerr effect (MOKE) technique to measure the hysteresis loops in ultrathin TmIG (i.e., 3.5 nm and 2.3 nm)/Pt bilayers. By combining optical and transverse magnetoresistivity measurements, we directly separate the SH-AH and SH-TH contributions to the transverse resistivity. We find that the topological Hall resistivity of the ultrathin TmIG (2.3 nm)/Pt bilayer is considerably larger than previously estimated values. By removing a “threshold field” artificially imposed by the lower-bound model previously used, our study suggests that skyrmions in TmIG/Pt bilayers can be stabilized at both near-zero external

\* Authors to whom correspondence should be addressed.  
elaineli@physics.utexas.edu, yang.1006@osu.edu

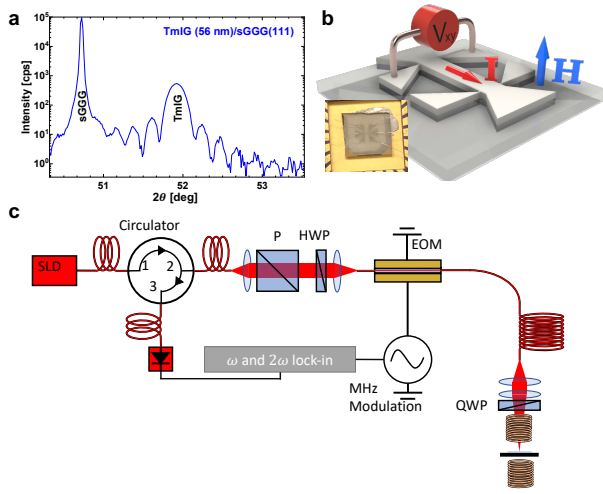


FIG. 1. Sample characterization and illustrations of the device and optical measurement. (a) XRD data of a typical TmIG/sGGG structure using this growth method is shown. The data presented is from a 56 nm TmIG film. (b) An illustration of the 6-contact device used in transport and MOKE measurements along with a photo of one of the wire bonded samples. (c) An illustration of the SaMOKE, a fiber-based Sagnac interferometer (more details in SM).

magnetic field and room temperature, extending the skyrmion phase diagram to a regime important for applications. Thus, our work represents a significant step for developing magnetic insulator thin films for nano-sized skyrmions and for accurate electrical read-outs of novel spin textures.

Epitaxial TmIG/Pt thin films were deposited by off-axis sputtering on  $\text{Gd}_{2.6}\text{Ca}_{0.4}\text{Ga}_{4.1}\text{Mg}_{0.25}\text{Zr}_{0.65}\text{O}_{12}$  (111) substrates (sGGG) from MTI Corporation. The differing TmIG and sGGG lattice constants, 12.324 [20, 26] and 12.480 Å respectively, result in a tensile strain and perpendicular magnetic anisotropy. X-ray diffraction (XRD) scan of a representative 56 nm TmIG film grown on sGGG is shown in Fig. 1a with clear Laue oscillations around the TmIG(444) peak, demonstrating the high quality of the epitaxial film. It has been shown in previous work that this growth method produces films without a magnetic dead layer at the TmIG/sGGG interface [22]. A 3.5 nm TmIG film provides a ferrimagnetically ordered reference sample away from the skyrmion phase at room temperature while a 2.3 nm TmIG film (with a Pt top layer) exhibits a strong SH-TH signal. After the TmIG growth, a 5 nm (2 nm) Pt layer was deposited on the 3.5 nm (2.3 nm) TmIG film. The thinner Pt layer thickness on top of the 2.3 nm TmIG increases the Hall signals. The bilayers were patterned into a  $100\ \mu\text{m} \times 400\ \mu\text{m}$  Hall bar geometry using photolithography and ion milling, as shown in Fig. 1b. The schematics of the SaMOKE set-up is shown in Fig. 1c and will be discussed in details later in the paper.

The bilayers were mounted on chip carriers and wire bonded for transport measurements as seen in Fig. 1b.

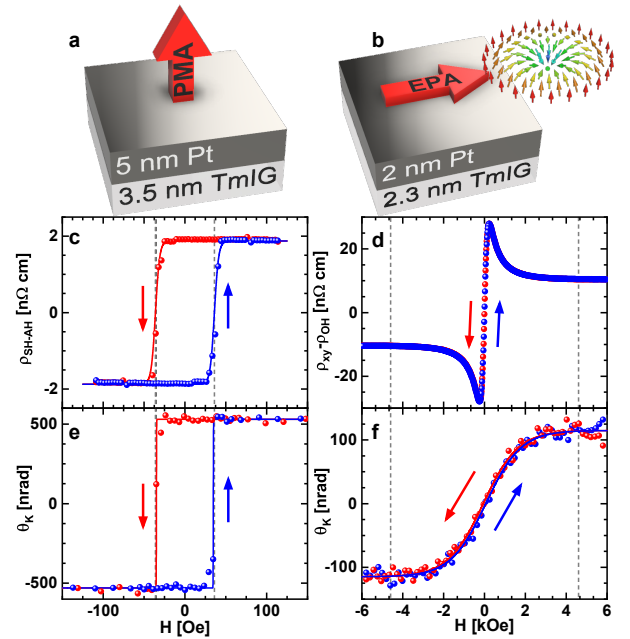


FIG. 2. Transverse resistivity and SaMOKE measurements as a function of an applied  $H$  field perpendicular to the film. The red arrows in (a) and (b) indicate the orientation of the magnetic easy axis in the 3.5 and 2.3 nm samples respectively. The layers indicate the thickness of Pt and TmIG films. An illustration of a skyrmion in (b) indicates the source of the SH-TH resistivity. Transverse resistivity from (c) TmIG (3.5 nm)/Pt (5 nm) and (d) TmIG (2.3 nm)/Pt (2 nm) bilayers. SaMOKE measurements from (e) TmIG 3.5 nm and (f) TmIG 2.3 nm bilayers. The solid curves in all panels are fits of the data. Red (blue) solid lines are fits to the red (blue) data. Vertical grey lines emphasize the agreement between optical and transport data.

Transverse DC Hall measurements were taken with  $I = 300\ \mu\text{A}$  as a function of the out-of-plane magnetic field in ambient conditions.

## II. RESULTS

### A. DC Hall Resistivity

The Hall resistivity data shown in Figs. 2c and d are taken from the 3.5 nm and 2.3 nm TmIG films, respectively, where the linear OH and paramagnetic backgrounds have been subtracted [34]. We fit the curves in all loops using the following equation,  $y(H) = a \tanh[(H - h_0)/(\Delta h)]$ , where  $a$  is the amplitude of the signal,  $H$  is the applied field,  $h_0$  the coercive field, and  $\Delta h$  the width of switching.

Because TmIG and sGGG are insulators, the resistivity measurements reflect interactions involving the charge current in the Pt layer and along the Pt/TmIG interface. The transverse resistivity potentially includes the follow-

ing terms

$$\rho_{xy} = \rho_{OH} + \rho_{AH,Pt} + \rho_{TH,Pt} + \rho_{SH-AH} + \rho_{SH-TH}, \quad (1)$$

where  $\rho_{OH}$  is the OH resistivity,  $\rho_{AH,Pt}$  and  $\rho_{TH,Pt}$  are the anomalous and topological Hall resistivities from Pt due to magnetic proximity effect [35, 36], and  $\rho_{SH-AH}$  and  $\rho_{SH-TH}$  are the SH-AH and SH-TH resistivities, respectively. It has been shown previously that there is negligible proximity induced magnetization in the Pt in these bilayers [20][37]. The spin Hall terms arise from the nonequilibrium proximity effect known as spin Hall magnetoresistance and not proximity induced magnetization [38]. In the following analyses, we neglect the  $\rho_{AH,Pt}$  and  $\rho_{TH,Pt}$  terms. We use the SH-AH and SH-TH effects to probe spin textures in the TmIG thin films and focus on how to independently quantify these two contributions in Fig. 2d in the rest of measurements and analyses.

The pronounced difference between the field-dependent transverse resistivity between the 3.5 and 2.3 nm TmIG originates from a transition from perpendicular to in-plane magnetic anisotropy as indicated in Fig. 2a-b and shown in Fig. 2c-d. For TmIG thicknesses 3 nm and above, the magnetization is out-of-plane dictated by the magnetocrystalline anisotropy. In contrast, in the 2.3 nm film the TmIG/Pt interfacial anisotropy becomes dominant and forces the easy-axis into the plane of the film [20, 26, 39]. More critical to electrical read-out of the topological spin textures is the emergence of the SH-TH effect, manifested as bumps in the Hall resistivity loops exceeding the value beyond saturation  $H$  field. This unusual resistivity generally originates from the increase of Berry phase of charge and spin currents interacting with topological spin textures [2-4, 11, 40, 41], indicated by the illustration of the skyrmion in Fig. 2b.

## B. Magneto Optical Determination of Out of Plane Hysteresis

To capture the magnetic-field dependence of the very small magnetic moment in TmIG thin films, we apply the SaMOKE technique with a  $\sim 15$  nrad sensitivity in the Kerr angle. The SaMOKE measurements were performed using a 1550 nm source in the zero-area loop configuration (Fig. 1c) [34, 42-44]. The Sagnac interferometer, a type of same path interferometry, also ensures that any signals measured originate from broken time-reversal symmetry. This feature ensures that the small Kerr angles measured in this work are of magnetic origin. The measurements were taken in the polar geometry by passing the probe beam through one electromagnet pole. The spot size used for these measurements was  $\sim 100 \mu\text{m}$  in diameter.

The SaMOKE data are displayed in Figs. 2e and f, representing an average of 50 and 200 field sweeps respectively. The SaMOKE data from the 3.5 nm sample shown in Fig. 2e have good agreement with the resistivity

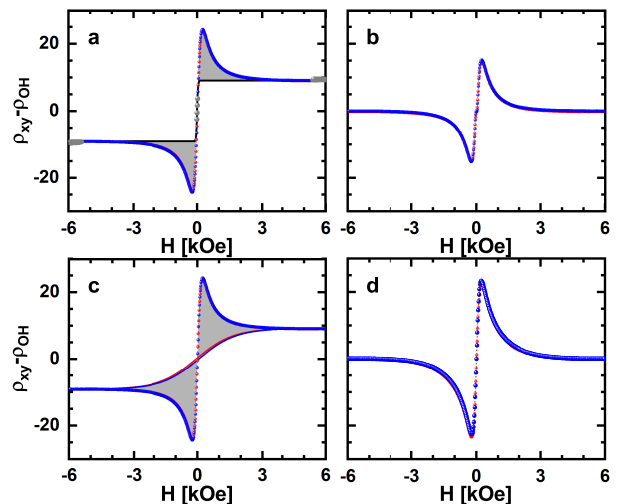


FIG. 3. Comparison between two SH-AH and SH-TH separation methods. All resistivity values are shown in  $\text{n}\Omega \text{ cm}$ . (a) The transverse resistivity is shown (red and blue) with the transport informed SH-AH fit (black) using the near zero field and high field data, emphasized in gray. (b) The SH-TH data derived from the transport data fit. Shown as gray fill in (a). (c) The transverse resistivity is shown with the MOKE derived SH-AH functions shown as solid curves. The SH-TH contributions are shown as the shaded regions (d) The MOKE informed SH-TH results.

measurements in Fig. 2c in the saturation and coercive fields [34]. This suggests the TmIG/Pt Kerr signal at 1550 nm is proportional to the magnetization.

The SaMOKE data for the 2.3 nm TmIG sample is presented in Fig. 2f, where the solid lines are fits to the data. A small hysteresis loop along with a larger saturation field as well as a small coercivity of  $63 \pm 32$  Oe is observed in the MOKE data. The 2.3 nm film exhibits in-plane anisotropy. Thus, the polar MOKE signal is necessarily small at near-zero external field. Furthermore, the ultrathin TmIG film yields a small SaMOKE signal of  $\sim 115$  nrad beyond the saturation field.

## III. DISCUSSION

We now compare two methods of quantifying the SH-AH resistivity in order to extract the SH-TH contribution. The first method follows a previous study by approximating the SH-AH (black curve in Fig. 3a) using a  $\tanh(H/\Delta h)$  function [20]. In this model, The SH-AH in the low-field regime is determined by fitting the  $\tanh$  to several data points (grey points near zero field) and, in the high-field regime, the measured resistivity beyond the saturation field (grey points  $> 5$  kOe). To extract the SH-TH contribution, the SH-AH fit (black curve) is subtracted from the measured values (red and blue data) in Fig. 3a. The difference yields the lower bound (LB) SH-TH,  $\rho_{SH-AH}^{LB}$  displayed in Fig. 3b. This fitting procedure inherently assumes there is no SH-TH contribu-

tion in the low-field regime. In a previous study [20], it has already been emphasized that this upper bound SH-AH model cannot accurately describe how rapidly (or gradually) the magnetization is reversed near zero field. In the second method, the experimentally measured SaMOKE loop was scaled to match the resistivity data in the high field regime (Fig. 3c). The difference between them yields the MOKE-informed SH-TH  $\rho_{SH-TH}^M$  as displayed in Fig. 3d.

To highlight the differences between the two analysis methods, we re-plot Figs. 3b and d within  $\pm 250$  Oe in Fig. 4a. The green line with a slope  $\sim 204$  n $\Omega$  cm/kOe demonstrates the linearity of  $\rho_{SH-TH}^M$  at small fields. First, the maximum value of  $\rho_{SH-TH}^M$  is significantly larger than the max  $\rho_{SH-TH}^{LB}$ . At 50 Oe, the extracted SH-TH value is  $\sim 4$  times of that from the first method. The SH-TH resistivity was shown to be proportional to the density of skyrmions in a previous work in the isolated skyrmion regime [4]. Secondly and more importantly, our analysis reveals that topological spin textures can form at near-zero applied field and generate a reasonably large spin magnetoresistive response.

To estimate the skyrmion density  $n_{sk}$  using the SH-TH resistivity results, we first explored a common method,  $n_{sk} = \rho_{SH-TH}/P R_{OH} \phi_0$  [2-4, 11, 23], where  $P$  is the spin polarization of the current in the Pt layer.  $R_{OH}$  is the OH resistivity coefficient of Pt which is determined experimentally from  $R_{OH} = \rho_{OH}/H$ . If we assume  $P = 0.1$  [23], an unrealistic skyrmion density of  $\sim 208,500 \mu\text{m}^{-2}$  is obtained at  $\sim 227$  Oe. This equation is derived from a single band model for electrons moving through spin textures and skyrmions [2, 40, 41]. These assumptions do not hold for TmIG/Pt bilayers where the Pt is not magnetic and the charges only interact with the skyrmions through spin Hall magneto-resistance mechanisms.

We adapt a formalism used to describe transport properties for a bilayer consisting of a magnetic insulator and a heavy metal (e.g.  $\text{Y}_3\text{Fe}_5\text{O}_{12}/\text{Pt}$  [38]) although we do not apply the derivation of any specific interfacial effects. This general formulation may take into account (i) the magneto-resistance effects generated by the magnetic layer, (ii) the spin accumulation at the interface, and (iii) inverse spin Hall effect. The SH-AH resistivity is described by a general expression:  $\rho_{SH-AH} \approx -\Delta\rho_2 m_z$ . We extract  $\rho_{SH-AH}$  from transport measurements and  $m_z$  from our SaMOKE measurement. We then determine  $\Delta\rho_2$ , which describes the interfacial effects. In the high field regime beyond the saturation, one can assume that the out of plane magnetization unit vector  $m_z = 1$ .  $\Delta\rho_2$  is approximated as the scaling constant used in Fig. 3c. In the low field regime,  $m_z$  as a function of magnetic field is obtained from SaMOKE measurements.

Similarly, we can describe the SH-TH resistivity by  $\rho_{SH-TH} \approx -\Delta\rho_2 m_{sk}$ , where  $m_{sk}$  represents the effective field generated by the skyrmions. It can be related to skyrmion density via  $m_{sk} = n_{sk} \phi_0 / 4\pi M_s$ , where

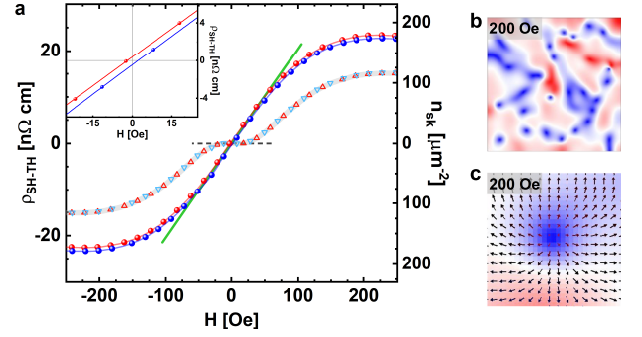


FIG. 4. Skyrmion density and micromagnetic estimations. (a) Comparison of the lower-bound SH-TH (red and blue triangles) and the MOKE-informed SH-TH (red and blue circles) (left-axis) and the MOKE-informed SH-TH resistivity (left-axis) and estimated skyrmion density (right-y axis). The dashed horizontal line indicates zero resistivity and skyrmion density from the lower-bound model for  $\rho_{SH-TH}$ . The green line shows the approximate linearity of  $\rho_{SH-TH}^M$  at small fields. The inset shows the non-zero coercive field in  $\rho_{SH-TH}^M$ . (b) shows a representative result of our simulations at 200 Oe. There are clear individual skyrmions at 200 Oe. (c) A zoom-in panel around one of the small circular patterns in our simulations, showing a Néel-like spin texture. Red indicates out of the plane magnetization and blue into the plane.

$\phi_0 = 2\pi\hbar/e$  is the magnetic flux quantum. We then estimate the skyrmion density with the following equation in Gaussian units,

$$n_{sk} \approx \frac{4\pi\rho_{SH-TH}M_s}{\phi_0\Delta\rho_2}, \quad (2)$$

where  $M_s$  is the saturation magnetization and  $\Delta\rho_2$  is approximated as a constant and determined from  $\rho_{SH-AH}(H > H_{sat})$ .  $M_s$  is not easily determined for these ultrathin films. We use the  $M_s$  of the sputtering target  $\sim 115$  emu/cm<sup>3</sup> as an approximation. The maximum density calculated using this method is  $n_{sk} \approx 179 \mu\text{m}^{-2}$  at  $\sim 227$  Oe for  $\rho_{SH-TH}^M = 23.4$  n $\Omega$  cm. We note that this estimated skyrmion density agrees well with micromagnetic simulations (details included in SI) [23]. The skyrmion density varies approximately linearly with the applied magnetic field over a small field range up to  $\sim 50$  Oe. The small hysteresis indicates the possibility of a small but finite skyrmion density at zero-field evidenced in  $\rho_{SH-TH}^M$ , as seen in the inset of Fig. 4a.

We explored a different method for estimating skyrmion density using micromagnetic simulations [45]. The simulations closely follow those performed in the work of Shao *et al.* [23]. There are several parameters that have not been measured in our series of ultrathin TmIG films for thicknesses less than 3 nm TmIG. We adapt the parameters for similar TmIG films with a Pt over-layer [23, 46] and assume an in-plane easy axis. Representative simulation results are shown in 4b at an external perpendicular field 200 Oe. The 200 Oe panel displays a skyrmion density of approximately 108 skyrmions/ $\mu\text{m}^2$ ,

which is of the same order of magnitude estimated in the main text. Our simulations show a slow approach to saturation after the 200 Oe. In 4c, a zoom-in panel of a small circular pattern in our simulations shows a skyrmion-like spin texture. Details of our calculation are given in the supplementary information [34].

In summary, we have performed sensitive MOKE measurements on ultrathin TmIG/Pt bilayers, where a sizable SH-TH signal has been attributed to skyrmion formation. By evaluating the SH-AH contribution more accurately than previously possible, we find that skyrmions can be stable at near-zero applied field in TmIG/Pt bilayers, extending the skyrmion phase diagram beyond those based only on transport measurements. While an estimate of the skyrmion density is provided, we acknowledge this estimate may not be accurate in absence of a full theory. Estimating skyrmion density from transport data is known to be a challenging problem especially when the interaction between skyrmions is not negligible [4]. Future experiments capable of imaging skyrmions with  $\sim$

10 nm radius are necessary to further establish the correlation between electrical signal and skyrmion density.

## ACKNOWLEDGEMENTS

This research was primarily supported by the National Science Foundation through the Center for Dynamics and Control of Materials: an NSF MRSEC under Cooperative Agreement No. DMR-1720595, and the Center for Emergent Materials, an NSF MRSEC under Grant No. DMR-2011876. Additional support was provided by the Welch Foundation F-1662. Facilities provided by MRSEC DMR-1720595 and by NSF MRI DMR-2019130 are gratefully acknowledged. Partial funding for L. J. Chang while visiting UT-Austin was provided by a Portugal-UT collaboration grant. The collaboration between S.F. Lee and X. Li is facilitated by the AFOSR grant FA2386-21-1-4067.

- 
- [1] C. Back, V. Cros, H. Ebert, K. Everschor-Sitte, A. Fert, M. Garst, T. Ma, S. Mankovsky, T. Monchesky, M. Mostovoy, *et al.*, *Journal of Physics D: Applied Physics* **53**, 363001 (2020).
- [2] A. Neubauer, C. Pfleiderer, B. Binz, A. Rosch, R. Ritz, P. Niklowitz, and P. Böni, *Physical review letters* **102**, 186602 (2009).
- [3] D. Maccariello, W. Legrand, N. Reyren, K. Garcia, K. Bouzehouane, S. Collin, V. Cros, and A. Fert, *Nature nanotechnology* **13**, 233 (2018).
- [4] M. Raju, A. Petrović, A. Yagil, K. Denisov, N. Duong, B. Göbel, E. Şaşıoğlu, O. Auslaender, I. Mertig, I. Rozhansky, *et al.*, *Nature communications* **12**, 1 (2021).
- [5] U. K. Roessler, A. Bogdanov, and C. Pfleiderer, *Nature* **442**, 797 (2006).
- [6] S. Mühlbauer, B. Binz, F. Jonietz, C. Pfleiderer, A. Rosch, A. Neubauer, R. Georgii, and P. Böni, *Science* **323**, 915 (2009).
- [7] N. Kanazawa, Y. Onose, T. Arima, D. Okuyama, K. Ohoyama, S. Wakimoto, K. Kakurai, S. Ishiwata, and Y. Tokura, *Physical review letters* **106**, 156603 (2011).
- [8] J. Gallagher, K. Meng, J. Brangham, H. Wang, B. Esser, D. McComb, and F. Yang, *Physical review letters* **118**, 027201 (2017).
- [9] W. Jiang, P. Upadhyaya, W. Zhang, G. Yu, M. B. Jungfleisch, F. Y. Fradin, J. E. Pearson, Y. Tserkovnyak, K. L. Wang, O. Heinonen, *et al.*, *Science* **349**, 283 (2015).
- [10] M. Raju, A. Yagil, A. Soumyanarayanan, A. K. Tan, A. Almoalem, F. Ma, O. Auslaender, and C. Panagopoulos, *Nature communications* **10**, 696 (2019).
- [11] K. Zeissler, S. Finizio, K. Shabazi, J. Massey, F. Al Ma'Mari, D. M. Bracher, A. Kleibert, M. C. Rosamond, E. H. Linfield, T. A. Moore, *et al.*, *Nature nanotechnology* **13**, 1161 (2018).
- [12] M. Sapozhnikov, N. Gusev, S. Gusev, D. Tatarskiy, Y. V. Petrov, A. Temiryazev, and A. Fraerman, *Physical Review B* **103**, 054429 (2021).
- [13] C. Moreau-Luchaire, C. Moutafis, N. Reyren, J. Sampaio, C. Vaz, N. Van Horne, K. Bouzehouane, K. Garcia, C. Deranlot, P. Warnicke, *et al.*, *Nature nanotechnology* **11**, 444 (2016).
- [14] O. Boule, J. Vogel, H. Yang, S. Pizzini, D. de Souza Chaves, A. Locatelli, T. O. Mentes, A. Sala, L. D. Buda-Prejbeanu, O. Klein, *et al.*, *Nature nanotechnology* **11**, 449 (2016).
- [15] F. Büttner, I. Lemesch, and G. S. Beach, *Scientific reports* **8**, 4464 (2018).
- [16] H. Wang, C. Du, Y. Pu, R. Adur, P. Hammel, and F. Yang, *Physical Review B* **88**, 100406 (2013).
- [17] S. Vélez, J. Schaab, M. S. Wörnle, M. Müller, E. Gradauskaite, P. Welter, C. Gutgsell, C. Nistor, C. L. Degen, M. Trassin, *et al.*, *Nature communications* **10**, 4750 (2019).
- [18] L. Caretta, E. Rosenberg, F. Büttner, T. Fakhru, P. Gargiani, M. Valvidares, Z. Chen, P. Reddy, D. A. Muller, C. A. Ross, *et al.*, *Nature communications* **11**, 1090 (2020).
- [19] A. J. Lee, A. S. Ahmed, J. Flores, S. Guo, B. Wang, N. Bagués, D. W. McComb, and F. Yang, *Physical review letters* **124**, 107201 (2020).
- [20] A. S. Ahmed, A. J. Lee, N. Bagués, B. A. McCullian, A. M. Thabt, A. Perrine, P.-K. Wu, J. R. Rowland, M. Randeria, P. C. Hammel, *et al.*, *Nano letters* **19**, 5683 (2019).
- [21] A. J. Lee, S. Guo, J. Flores, B. Wang, N. Bagués, D. W. McComb, and F. Yang, *Nano Letters* **20**, 4667 (2020).
- [22] A. J. Lee, S. Guo, A. S. Ahmed, and F. Yang, *Physical Review B* **102**, 174434 (2020).
- [23] Q. Shao, Y. Liu, G. Yu, S. K. Kim, X. Che, C. Tang, Q. L. He, Y. Tserkovnyak, J. Shi, and K. L. Wang, *Nature Electronics* **2**, 182 (2019).
- [24] H. Wang, C. Du, P. C. Hammel, and F. Yang, *Physical review letters* **113**, 097202 (2014).

- [25] Y. Cheng, A. J. Lee, G. Wu, D. V. Pelekhov, P. C. Hammel, and F. Yang, *Nano Letters* **20**, 7257 (2020).
- [26] C. Tang, P. Sellappan, Y. Liu, Y. Xu, J. E. Garay, and J. Shi, *Physical Review B* **94**, 140403 (2016).
- [27] Q. Shao, C. Tang, G. Yu, A. Navabi, H. Wu, C. He, J. Li, P. Upadhyaya, P. Zhang, S. A. Razavi, *et al.*, *Nature communications* **9**, 3612 (2018).
- [28] C. O. Avci, A. Quindeau, C.-F. Pai, M. Mann, L. Caretta, A. S. Tang, M. C. Onbasli, C. A. Ross, and G. S. Beach, *Nature materials* **16**, 309 (2017).
- [29] C. O. Avci, E. Rosenberg, M. Baumgartner, L. Beran, A. Quindeau, P. Gambardella, C. A. Ross, and G. S. Beach, *Applied Physics Letters* **111**, 072406 (2017).
- [30] C. O. Avci, E. Rosenberg, L. Caretta, F. Büttner, M. Mann, C. Marcus, D. Bono, C. A. Ross, and G. S. Beach, *Nature nanotechnology* **14**, 561 (2019).
- [31] X. Yu, J. P. DeGrave, Y. Hara, T. Hara, S. Jin, and Y. Tokura, *Nano letters* **13**, 3755 (2013).
- [32] Furthermore, it has been shown that spin structures with trivial topology, such as static domain walls, do not contribute to topological Hall and SH-TH signals [47].
- [33] Y. Cheng, S. Yu, M. Zhu, J. Hwang, and F. Yang, *APL Materials* **9**, 051121 (2021).
- [34] See supplemental material at [url will be inserted by publisher] for a description of film growth, experimental apparatuses, data with linear backgrounds, fitting parameters, and simulation information.
- [35] J. J. Bauer, P. Quarterman, A. J. Grutter, B. Khurana, S. Kundu, K. A. Mkhoyan, J. A. Borchers, and C. A. Ross, *Physical Review B* **104**, 094403 (2021).
- [36] S. Ding, Z. Liang, C. Yun, R. Wu, M. Xue, Z. Lin, A. Ross, S. Becker, W. Yang, X. Ma, *et al.*, *Physical Review B* **104**, 224410 (2021).
- [37] A recent paper discussing the possible presence of proximity induced magnetism in Pt grown on TmIG has come to our attention during the review process [48]. Since this effect is very dependent on the interface and therefore the growth conditions we believe that our conclusion is valid. If there is a proximity contribution, our method should still be valid in separating the anomalous and topological contributions to the resistivity. Those terms which we designate as  $\rho_{SH-AH}$  and  $\rho_{SH-TH}$  could then just be reinterpreted as a sum of terms.
- [38] Y.-T. Chen, S. Takahashi, H. Nakayama, M. Althammer, S. T. Goennenwein, E. Saitoh, and G. E. Bauer, *Physical Review B* **87**, 144411 (2013).
- [39] C. Wu, C. Tseng, Y. Fanchiang, C. Cheng, K. Lin, S. Yeh, S. Yang, C. Wu, T. Liu, M. Wu, *et al.*, *Scientific reports* **8**, 11087 (2018).
- [40] N. Nagaosa and Y. Tokura, *Nature nanotechnology* **8**, 899 (2013).
- [41] P. Bruno, V. Dugaev, and M. Taillefumier, *Physical review letters* **93**, 096806 (2004).
- [42] J. Xia, P. T. Beyersdorf, M. M. Fejer, and A. Kapitulnik, *Applied physics letters* **89**, 062508 (2006).
- [43] A. Fried, M. Fejer, and A. Kapitulnik, *Review of Scientific Instruments* **85**, 103707 (2014).
- [44] R. McLaughlin, D. Sun, C. Zhang, M. Groesbeck, and Z. V. Vardeny, *Physical Review B* **95**, 180401 (2017).
- [45] M. J. Donahue and M. Donahue, *OOMMF user's guide, version 1.0* (US Department of Commerce, National Institute of Standards and Technology, 1999).
- [46] A. J. Lee, A. S. Ahmed, B. A. McCullian, S. Guo, M. Zhu, S. Yu, P. M. Woodward, J. Hwang, P. C. Hammel, and F. Yang, *Physical Review Letters* **124**, 257202 (2020).
- [47] K.-J. Kim, M. Mochizuki, and T. Ono, *Applied Physics Express* **12**, 053006 (2019).
- [48] A. Bose, R. Jain, J. J. Bauer, R. A. Buhrman, C. A. Ross, and D. C. Ralph, *Physical Review B* **105**, L100408 (2022).